PFC/JA-85-13

THE RIPPLED-FIELD MAGNETRON
(CROSS-FIELD FREE ELECTRON LASER)

F. Hartemann
G. Bekefi
R.E. Shefer

Plasma Fusion Center
Massachusetts Institute of Technology
Cambridge, Massachusetts 02139 USA

March 1985

THE RIPPLED-FIELD MAGNETRON

(CROSS-FIELD FREE ELECTRON LASER)

F. Hartemann,† G. Bekefi, and R.E. Shefer

Department of Physics and Research Laboratory of Electronics

Massachusetts Institute of Technology

Cambridge, Massachusetts 02139

ABSTRACT

Millimeter wave emission from the rippled-field magnetron (cross-field free electron laser) is investigated experimentally and theoretically. In this device, electrons move in quasi-circular orbits under the combined action of a radial electric field, a uniform axial magnetic field, and a radial, azimuthally periodic wiggler magnetic field. In excess of 300kW of RF power is observed in two narrow spectral lines whose frequency can be tuned continuously from ∿25GHz to ∿50GHz by variation of the axial magnetic field. The observations are interpreted as a free electron laser type of instability, associated with a resonance in the particle motion, which is shown to occur when $2k_w v_o \simeq (\Omega_o/\gamma_o)\sqrt{1-(\omega_p/\Omega_o)^2}$, where k_w is the wiggler wavenumber, v_o is the azimuthal electron velocity, Ω_o is the relativistic cyclotron frequency in the axial magnetic field, ω_p is the relativistic plasma frequency, and $\gamma_o=[1-(v_o/c)^2]^{-\frac{1}{2}}$.

†Permanent address: Laboratoire de Physique des Gaz et des Plasmas, Université Paris XI, Centre Scientifique d'Orsay, France.

I. INTRODUCTION

Many studies have been reported of linear[1] free electron lasers (FELs) in which short wavelength radiation is produced when electrons moving in essentially straight lines interact with a spatially periodic wiggler magnetic field. Recently, novel circular geometry FELs has been explored both theoretically[2,3,4,5] and experimentally[6,7,8] in which a rotating, relativistic electron ring interacts with an azimuthally periodic wiggler field produced by samarium cobalt magnets placed interior and exterior to the beam. The potential advantages of such systems include a longer effective interaction region, a more compact geometrical configuration, and internal feedback resulting from the recirculation of the electromagnetic wave. This last feature may mean that the device can operate as an oscillator rather than an amplifier, as in the case of linear FELs. Moreover, calculations show that the instability growth rates are high[5] and comparable to those of a gyrotron.

In the experiments to date, two principal methods have been used to generate the rotating electron beam. The first experiments[6] employed a diode configuration similar to that used in relativistic magnetrons. Here the electrons perform $\vec{E}\times\vec{B}$ drifts around the azimuth in the presence of a radial electric field and an axial magnetic field. Addition of an azimuthally periodic magnetic field then results in a circular FEL called the Rippled-Field Magnetron or Cross-Field FEL, the latter term being sometimes reserved for the case of a tenuous[3] rotating ring, the former for the case of dense beams[2,4] at or near Brillouin equilibrium.

In an alternate configuration,[7,8] the rotating electron beam is produced by passing a hollow, nonrotating electron beam through a narrow magnetic cusp. In this manner, the $e\vec{v}_z\times\vec{B}_r$ force at the center of the cusp effectively converts the axial beam velocity into rotational velocity downstream of the cusp region. If the cusp is symmetric, the downstream beam performs simple axis encircling

cyclotron orbits with a gyroradius equal to the radius of the beam on the upstream side of the cusp. This configuration has been discussed in detail elsewhere,[7,8] and lies outside the subject matter of this paper.

In this paper we describe a continuation of our earlier experiments[6] on the rippled-field magnetron and new computations aimed at interpreting the observations. In section II we describe the experiments in which more than 300 kW of RF power is observed in two narrow spectral lines whose frequency can be continuously tuned from ∿25GHz to ∿50GHz by variation of the axial magnetic field. In section III we discuss computations of the dispersion equation of the instability. We show that the observations can be interpreted as an interaction between a cyclotron-like mode on the electron beam upshifted by the wiggler periodicity, and an electromagnetic wave, at and near a resonance in the particle motion found to occur when $2k_w v_o \simeq (\Omega_o/\gamma_o)\left[1-(\omega_p/\Omega_o)^2\right]^{\frac{1}{2}}$. Here $k_w = 2\pi/\ell_w$ is the wiggler wavenumber with ℓ_w as its periodicity; $\Omega_o = eB_o/m_o\gamma_o$ is the relativistic electron cyclotron frequency $\omega_p^2 = n_o e^2/\gamma_o m_o \varepsilon_o$ is the relativistic electron plasma frequency, $\gamma_o = \left[1-(v_o/c)^2\right]^{-\frac{1}{2}}$ is the relativistic energy factor, and v_o is the azimuthal electron velocity. The existence of the aforementioned resonance is substantiated by computer simulations which will also be discussed. Section IV summarizes the findings.

II. EXPERIMENTS

The device is illustrated schematically in Fig. 1. It comprises a smooth cylindrical cathode of radius r_c enclosing a smooth coaxial cylindrical anode of radius r_a. The electrons, emitted from the cathode by field emission[9] are subjected simultaneously to two quasi-steady fields acting at right angles to one another: a uniform, axial magnetic field produced by magnetic coils, and a radial electric field generated by applying a voltage V between the electrodes. In the absence of the wiggler field, a space-charge cloud

forms, partially filling the interaction gap $(r_c - r_a)$; the electrons undergo azimuthal rotation having a sheared, radially dependent velocity $v_o(r) = E_o(r)/B_o(r)$ where $E_o(r)$ and $B_o(r)$ include the externally applied and self-fields.

Superimposed on the $\vec{E}_o$ and $\vec{B}_o$ fields is an azimuthally periodic magnetic wiggler field $\vec{B}_w$, which perturbs the Brillouin flow of the electron stream. Subject to the requirement that $\nabla\cdot\vec{B}_w = \nabla\times\vec{B}_w = 0$, the field in the vacuum gap between the cathode and anode is calculated to be,

$$\vec{B}_w = \hat{r}\,\frac{B_{ow}}{2}\cos(N\theta)\left[\left(\frac{r}{r_c}\right)^{N-1} + \left(\frac{r_a}{r}\right)^{N+1}\right]\left[\frac{r_c}{r_a}\right]^{(N^2-1)/2N}$$

$$-\hat{\theta}\,\frac{B_{ow}}{2}\sin(N\theta)\left[\left(\frac{r}{r_c}\right)^{N-1} - \left(\frac{r_a}{r}\right)^{N+1}\right]\left[\frac{r_c}{r_a}\right]^{(N^2-1)/2N}$$

where $\hat{r}$ and $\hat{\theta}$ are unit vectors in the radial and azimuthal directions, respectively. $N=\pi(r_c+r_a)/\ell_w$ is the number of spatial periods and ℓ_w is the linear periodicity defined midway in the gap. B_{ow} is the amplitude of the radial component of field at a distance $r=r_o\equiv(r_c^{N-1}r_a^{N+1})^{1/(2N)}$ where the azimuthal field component vanishes (which is roughly midway between the cathode and anode). We see that near the center of the gap the wiggler field is primarily radial and is thus transverse to the electron flow velocity $\vec{v}_o=\vec{E}_o\times\vec{B}_o/B_o^2$, as is the case in conventional free electron lasers.

In our device, the wiggler magnetic field is produced by an assembly of samarium-cobalt[10] bar magnets. The magnets are positioned behind smooth stainless steel electrodes and held in place in grooved aluminum cylinders. Once the system is assembled, the inner electrode (anode) is connected to the positive terminal of the pulsed, high voltage accelerator. The outer field-emission cathode is grounded. Table I gives a summary of the diode dimensions and

experimental parameters, and Table II gives data concerning the permanent magnet system. For N=12 periods around the azimuth, four magnets per period are used; for n=24, two magnets per period are employed. Details of magnet placement are described elsewhere.[6]

Figure 2 shows an overall view of the experimental arrangement. The electric field between cathode and anode is provided by the Physics International Pulserad 110A high voltage facility. The axial magnetic field is generated by two pulsed magnetic field coils surrounding, and coaxial with, the cylindrical electrodes. Typical current-voltage characteristics of the system as a function of the axial magnetic field are shown in Fig. 3. In all cases the magnetic field exceeds the critical field required for magnetic insulation.[9]

The radiation generated in the rippled-field magnetron is allowed to leak out through the Pyrex window seen in Fig. 2. The radiation leaving the Pyrex window in a given direction is received with a horn antenna and rectified in a calibrated crystal detector. To obtain the total emitted power[9] in a given microwave frequency band, we make an angular scan of the radiation pattern of the transmitter, derive its gain and use the familiar radar formula.[9]

The frequency spectra are measured in one of two ways, by means of a solid state or waveguide dispersive line and by a millimeter wave grating spectrometer.[11] A dispersive line gives the spectrum in a single firing of the accelerator, but has poorer spectral resolution. The grating spectrometer has much better resolution. However, since the spectra must be assembled from successive shots, data acquisition is tedious and for that reason the spectrometer has been used sparingly, and then mostly to obtain detailed spectral line widths.

Figure 4 shows the total radiated power in the 26-40GHz frequency band, as a function of the axial magnetic field, for a wiggler having a periodicity ℓ_w=2.53cm(N=12) and an amplitude B_{ow}=1.96kG. The peaks in emitted power exceed

300kW. When the wiggler is turned off (by removing the samarium-cobalt magnets from their grooved aluminum cylinders), the emitted power falls by more than a factor of 20.

Spectral characteristics of the emitted radiation, obtained with the grating spectrometer are illustrated in Fig. 5. The measured line width at the half power points is ~2.2GHz (the instrument line width is ~1.0GHz). The lower part of Fig. 5 shows that in the absence of the wiggler, the level of radiation has fallen by more than three orders of magnitude; the emission is broad-band and shows no narrow spectral features.

The radiation frequency of the spectral line shown in Fig. 5 increases linearly with the strength of the axial magnetic field. This continuous frequency tuning from 32GHz to 45GHz is illustrated in Fig. 6. Figure 7 shows that in addition to the spectral line referred to in Figs. 5 and 6, there is a lower frequency branch which has similar tuning characteristics with magnetic field as the upper branch. Figure 7 also shows the experimental results obtained when the wiggler periodicity N equals 24 (see Table II). We see that doubling the periodicity from N=12 to N=24 does not cause an appreciable change in the radiation frequency. This is quite unlike a conventional FEL in which doubling the periodicity would cause a doubling of the frequency. This behavior of the rippled field magnetron and the tuning characteristics illustrated in Figs. 6 and 7 are in agreement with the computed dispersion characteristics discussed in Section III.

III. THEORY

Electron Dynamics

Because of the small gap width $[d=(r_c-r_a)<<(r_c+r_a)]$ of the rippled-field magnetron, the planar model illustrated in Fig. 8 is an adequate representation. For purposes of simplicity we first assume that the cathode-anode gap

is filled with a tenuous electron beam having a spatial density profile $n_o(x)$, and drifting (in the absence of the wiggler) with velocity $\vec{v}_o = \hat{z}\, E_o/B_o$ under the combined action of the crossed electric and magnetic fields $\hat{x}E_o$ and $\hat{y}B_o$, respectively. We then have

$$\left.\begin{aligned} \vec{E}_o &= (V/d)\hat{x} \\ \vec{B}_o &= B_o\hat{y} \\ \vec{v}_o &= (E_o/B_o)\hat{z} \quad , \quad \beta_o = v_o/c \\ \gamma_o &= (1 - \beta_o^2)^{-\frac{1}{2}} \end{aligned}\right\} \tag{1}$$

where V is the voltage applied between the anode and the cathode, γ_o the relativistic energy factor and $n_o(x)$ a given density profile corresponding to the beam shape. The assumption of a tenuous beam implies that $f^2(x) \equiv \omega_p^2(x)/\Omega_o^2 << 1$. Here, $\Omega_o = eB_o/\gamma_o m_o$ and $\omega_p^2(x) = e^2 n_o(x)/\gamma_o m_o \varepsilon_o$ where Ω_o is the relativistic cyclotron frequency, and ω_p the relativistic plasma frequency.

We now consider the presence of the periodic wiggler field $\hat{x}B_w\cos(k_w z)$, where k_w is the wiggler wavenumber $k_w = 2\pi/\ell_w$. Under the assumption $B_w/B_o << 1$, we can write that

$$\vec{v} = v_o\hat{z} + \delta\vec{v} \quad , \quad \gamma = (1 - v^2/c^2)^{-\frac{1}{2}} = \gamma_o + \delta\gamma \tag{2}$$

with $|\delta\vec{v}| << v_o$ and $\delta\gamma << \gamma_o$, and obtain the equations of motion for the electron momentum $\vec{p}$:

$$\dot{p}_x = e\delta v_z B_o \tag{3a}$$

$$\dot{p}_y = -e\dot{z}B_w\cos(k_w z) \tag{3b}$$

$$\dot{p}_z = -e\delta v_x B_o + e\delta v_y B_w\cos(k_w z) \; . \tag{3c}$$

We note that one can solve (3b) exactly, with the result that:

$$\delta\dot{v}_x \simeq \Omega_o \delta v_z \tag{4a}$$

$$\delta\dot{v}_z \simeq -\Omega_o \delta v_x/\gamma_o^2 - \Omega_w^2 \sin(2k_w z)/2k_w \tag{4b}$$

where $\Omega_w = eB_w/\gamma_o m_o$. Now setting $z \simeq v_o t$, $\dot{z} \simeq v_o$, we obtain,

$$\delta\ddot{v}_z + (\Omega_o/\gamma_o)^2 \delta v_z \simeq -v_o \Omega_w^2 \cos(2k_w v_o t). \qquad (5)$$

This equation characterizes a system of eigen-frequency Ω_o/γ_o driven by the wiggler at $2k_w v_o$. The second harmonic of the wiggler appears due to the non-linear coupling $\delta v_y B_w \cos(k_w z)$ in the z-component of the Lorentz force. Of course such a system exhibits a resonance when $\Omega_o/\gamma_o = 2k_w v_o$.

Using the initial conditions $z(t=0)=0$, $\delta\vec{v}(t=0)=\vec{0}$ and the approximation $v_o t \simeq z$, leads to a steady rippled equilibrium:

$$\begin{aligned} \delta v_x(z) &= \Omega_o v_o R\left[\sin(2k_w z)/2k_w v_o - \Omega_o \sin(\Omega_o z/\gamma_o v_o)/\gamma_o\right] \\ \delta v_y(z) &= -\Omega_w \sin(k_w z)/k_w \\ \delta v_z(z) &= v_o R\left[\cos(2k_w z) - \cos(\Omega_o z/\gamma_o v_o)\right] \end{aligned} \qquad (6)$$

where

$$R = \Omega_w^2/\left(4k_w^2 v_o^2 - (\Omega_o^2/\gamma_o^2)\right), \quad (2k_w v_o \neq \Omega_o/\gamma_o) \qquad (7)$$

specifies the amplitude of the δv_x and δv_z components of the velocity. We observe that only these two components exhibit a resonant increase. The y component, which is transverse to the wiggler magnetic field and which plays the dominant role in conventional[1,2,3,4] FEL interactions, is not resonantly enhanced. Since our interest is focused on FEL-like interactions associated with the resonance enhancement, the y-directed oscillations will play no significant role in our derivation of the wave dispersion equations discussed below.

In order to check the analytical derivation of the rippled equilibrium, we have integrated the system of equations (3) numerically for different values of E_o, B_o, and ℓ_w. The single-particle simulation (Fig. 9 top) was generated for the following set of parameters: B_o=6.0kG, V=1.0MV, d=1.0cm, ℓ_w=1.0cm and a time step $\Delta t = 10^{-13}$s. This set corresponds to an "off resonance" situation where the hierarchy $\delta v_y >> \delta v_x$, δv_z remains valid. We obtain first order har-

monic motion at frequency $k_w v_o$ in the y-direction and a much smaller perturbation δv_x across the gap. A second simulation (Fig.9 bottom) was produced for B_o= 9.05kG, V=1.0MV, d=1.0cm, ℓ_w=1.0cm, and $\Delta t=10^{-13}$s, very close to the theoretical resonance $2k_w v_o=\Omega_o/\gamma_o$. Here, the situation is reversed; δv_x, $\delta v_z >> \delta v_y$, and we see that the frequency of the motion across the gap is twice that of the conventional undulatory motion. The anharmonicity in the y-direction is produced by the perturbation of velocity along the flow itself.

Figure 10 is obtained by fixing E_o and ℓ_w and varying B_o; for each value of B_o, we plot the maximum value of δv_x obtained after 2ns of simulation, with a time step of $\Delta t=10^{-14}$s and ℓ_w=1.0cm. The resonance occurs at 6.025kG for E_o=0.5MV cm^{-1} in agreement with analytical predictions. One notes the presence of a secondary peak at $k_w v_o=\Omega_o/\gamma_o$. This peak is probably a higher order effect which is not predicted analytically.

The aforementioned calculations and simulations refer to a tenuous beam $f\equiv\omega_p(x)/\Omega_o<<1$. When f is not small, we can use Poisson's equation and Ampere's theorem to take self-fields into account. We then find that the resonance shifts and acquires a value given by[12]

$$2k_w v_o = \frac{\Omega_o}{\gamma_o}\left(1-f^2\right)^{\frac{1}{2}} \qquad (8)$$

where in the general case v_o, γ_o and f are functions of position x within the beam. For perfect Brillouin equilibrium (f=1) the resonance vanishes. However, perfect Brillouin equilibrium is probably never achieved in practice, particularly not in the presence of a strong wiggler magnetic field, as in the case in our experiments.

Dispersion Relation

In our model the electromagnetic wave perturbation is taken to vary in the propagation direction z as exp(ikz-iωt). It is a transverse electromag-

netic wave polarized with the electric field $\vec{\tilde{E}}$ along the x axis of the coordinate system illustrated in Fig. 8. This choice of $\vec{\tilde{E}}$-field polarization assures coupling of the radiation field to the resonantly enhanced electron velocity component δv_x of Eq. (6). Thus, with the RF electric and magnetic fields given by $\vec{\tilde{E}}=\tilde{E}_x\hat{x}$ and $\vec{\tilde{B}}=\tilde{B}_y\hat{y}$, the particle equations of motion become

$$\begin{aligned} \dot{p}_x &= -eE_o - e\tilde{E}_x + e(v_o + \delta v_z + w_z)(B_o + \tilde{B}_y) \\ \dot{p}_z &= -e(\delta v_x + w_x)(B_o + \tilde{B}_y) \end{aligned} \tag{9}$$

where we have neglected terms associated with nonresonant motions that vary as $\cos(k_w z)$; $\vec{w}$ is the perturbed particle velocity due to the presence of the RF fields. After some straightforward algebra, we obtain a third-order description of the dynamics of an electron in the presence of the radiation fields:

$$\begin{aligned} &\gamma_o m_o\left(1 + \frac{\gamma_o^2}{c^2} v_o \delta v_z\right)\dot{w}_x = \\ &\qquad eB_o w_z - e(\tilde{E}_x - v_o\tilde{B}_y) + 2e\frac{E_o}{c^2}\delta v_x w_x - \gamma_o^2 e\frac{E_o}{c^2}\delta v_z w_z + e\delta v_z \tilde{B}_y \,, \\ &\gamma_o m_o\left(1 + \frac{\gamma_o^2}{c^2} v_o \delta v_z\right)\dot{w}_z = \\ &\qquad -e\frac{B_o}{\gamma_o^2} w_x + 2e\frac{E_o}{c^2}\delta v_x w_z + e\frac{E_o}{c^2}\delta v_z w_x + e\delta v_x\left(\frac{v_o}{c^2}\tilde{E}_x - \tilde{B}_y\right) \end{aligned} \tag{10}$$

We now express the velocity perturbation $\vec{w}$ as a function of the RF fields. We use Floquet's theorem, and express all quantities related to the radiation fields as

$$X(z,t) = \sum_{-\infty}^{+\infty} X_n \exp\left[i(k_n z - \omega t)\right] \quad , \quad k_n = k + nk_w \,. \tag{11}$$

Using the orthogonality of harmonic functions and the resonance condition, we obtain

$$\begin{aligned} \delta v_z &\equiv v_o \frac{R}{2}\left[\exp(i2k_w z) + \exp(-i2k_w z)\right] \\ \delta v_x &\equiv -i\gamma_o v_o \frac{R}{2}\left[\exp(i2k_w z) - \exp(-i2k_w z)\right] \,. \end{aligned} \tag{12}$$

After a considerable amount of algebra, one finds the soughtafter expressions for w_{xn} and w_{zn}:

$$w_{xn} = iD_n^2 \frac{e}{m_o} \tilde{E}_{xn} \left\{ \Omega_n^2/\gamma_o\omega + v_o^2 \frac{R^2}{4} D_{n+2}^2 \left[\Omega_n \left[Q_{n+2}^- \left(\Omega_{n+2} \frac{k_n}{\gamma_o\omega} + \Omega_o\Delta_n \right) \right. \right. \right.$$
$$\left. - \gamma_o q_o \left(\Omega_{n+2}\Delta_n + \frac{\Omega_o}{\gamma_o^2} \frac{k_n}{\gamma_o\omega} \right) \right] + \Omega_o \left[Q_{n+2}^- \left(\Omega_{n+2}\Delta_n + \frac{\Omega_o}{\gamma_o^2} \frac{k_n}{\gamma_o\omega} \right) \right.$$
$$\left. \left. \left. - q_o/\gamma_o \left(\Omega_{n+2} \frac{k_n}{\gamma_o\omega} + \Omega_o\Delta_n \right) \right] \right] \right\} \tag{13a}$$

$$w_{zn} = D_n^2 \frac{e}{m_o} \tilde{E}_{xn} \left\{ \Omega_o\Omega_n/\gamma_o^3\omega + v_o^2 \frac{R^2}{4} D_{n+2}^2 \left[\Omega_n \left[Q_{n+2}^- \left(\Omega_{n+2}\Delta_n + \frac{\Omega_o}{\gamma_o^2} \frac{k_n}{\gamma_o\omega} \right) \right. \right. \right.$$
$$-q_o/\gamma_o \left(\Omega_{n+2} \frac{k_n}{\gamma_o\omega} + \Omega_o\Delta_n \right) + \Omega_o/\gamma_o^2 \left[Q_{n+2}^- \left(\Omega_{n+2} \frac{k_n}{\gamma_o\omega} + \Omega_o\Delta_n \right) \right.$$
$$\left. \left. \left. - \gamma_o q_o \left(\Omega_{n+2}\Delta_n + \frac{\Omega_o}{\gamma_o^2} \frac{k_n}{\gamma_o\omega} \right) \right] \right] \right\} \tag{13b}$$

where $q_o = eE_o/m_o c^2$, $\Delta_n = (v_o/c^2) - (k_n/\omega)$; $\Omega_n = \omega - k_n v_o$; $Q_n^{\pm} = k_n(1+\gamma_o^2\beta_o^2) - \gamma_o^2\beta_o\omega/c \pm 2q_o$; $D_n^2 = 1/W_n^2$; $W_n^2 = \Omega_o^2/\gamma_o^2 - \Omega_n^2$.

The x-component of the wave equation relates the particle dynamics to the RF electric field, namely

$$(k_n^2 - \omega^2/c^2)\tilde{E}_{xn} = i\omega\mu_o j_{xn} \tag{14}$$

where $j_x = -e(n_o w_x + \delta n w_x + \eta\delta v_x)$ is the RF current density; η is the density perturbation caused by the radiation field, and δn the density perturbation associated with the resonant particle motion. Use of the continuity equation yields

$$\eta_n = n_o(k_n w_{zn} - i\alpha w_{xn})/\Omega_n \tag{15}$$

and

$$\delta n = n_o R \left(\frac{\alpha\gamma_o}{2k_w} - 1 \right) \cos(2k_w z) \tag{16}$$

where $\alpha(x)$ defines the scale length of the electron density gradient in the cathode-anode gap;

$$\alpha(x) = \frac{1}{n_o(x)} \frac{d}{dx} \left(n_o(x)\right) \tag{17}$$

Substituting Eqs. (13), (15), and (16) in Eq. (14) gives the dispersion equation:

$$\left[W_n^2\left(k_n^2 - \omega^2/c^2\right) - \Omega_n^2\omega_p^2/c^2\right] W_{n+2}^2 = \omega\gamma_o \frac{\omega_p^2}{c^2} C v_o^2 \frac{R^2}{4} \tag{18}$$

where the coupling term C is

$$\begin{aligned} C = \Bigg\{ & \Omega_n \left[Q_{n+2}^- \left(\Omega_{n+2} \frac{k_n}{\gamma_o \omega} + \Omega_o \Delta_n \right) - \gamma_o q_o \left(\Omega_{n+2} \Delta_n + \frac{\Omega_o}{\gamma_o^2} \frac{k_n}{\gamma_o \omega} \right) \right] \\ & + \Omega_o \left[Q_{n+2}^- \left(\Omega_{n+2} \Delta_n + \frac{\Omega_o}{\gamma_o^2} \frac{k_n}{\gamma_o \omega} \right) - \frac{q_o}{\gamma_o} \left(\Omega_{n+2} \frac{k_n}{\gamma_o \omega} + \Omega_o \Delta_n \right) \right] \\ & + \frac{1}{v_o \omega} \left(\frac{\alpha\gamma_o}{2k_w} + \frac{\alpha\gamma_o v_o}{\Omega_{n+2}} - 1 \right) \left[\frac{\Omega_n^2}{\gamma_o} \left(\Omega_o \frac{q_o}{\gamma_o} - \Omega_{n+2} Q_n^+ \right) + \frac{\Omega_o \Omega_n}{\gamma_o^3} \left(\Omega_{n+2} \gamma_o q_o - \Omega_o Q_n^+ \right) \right. \\ & \left. - \omega W_n^2 \left(\Omega_{n+2} \frac{k_n}{\gamma_o \omega} + \Omega_o \Delta_n \right) \right] + \frac{\gamma_o}{\omega} \frac{k_{n+2}}{\Omega_{n+2}} \left[\frac{\Omega_n^2}{\gamma_o} \left(\Omega_{n+2} \frac{q_o}{\gamma_o} - \frac{\Omega_o}{\gamma_o^2} Q_n^+ \right) \right. \\ & \left. + \frac{\Omega_o \Omega_n}{\gamma_o^3} \left(\frac{\Omega_o}{\gamma_o^2} \gamma_o q_o - \Omega_{n+2} Q_n^+ \right) - \omega W_n^2 \left(\Omega_{n+2} \Delta_n + \frac{\Omega_o}{\gamma_o^2} \frac{k_n}{\gamma_o \omega} \right) \right] \Bigg\} \end{aligned} \tag{19}$$

Despite the complexity of Eq. (18) its physical stucture can be readily understood. The left-hand side describes the interacting waves. The right-hand side is the wave coupling term which vanishes when the wiggler field B_w goes to zero. We examine the structure of the waves for the lowest order interaction n=0. Setting C=0 yields two waves

$$\omega = \left(k + 2k_w\right) v_o + \Omega_o/\gamma_o \tag{20}$$

which is a cyclotron-like beam mode[3,5,13] upshifted in frequency by the presence of the wiggler; and an electromagnetic wave[14] in the parallel plate waveguide filled with cold drifting electrons:

$$k^2c^2 = \omega^2 - \omega_p^2 \frac{(\omega - kv_o)^2}{(\omega-kv_o)^2-(\Omega_o/\gamma_o)^2} \tag{21}$$

The interaction between these waves is illustrated schematically in Fig. 11, showing two intersection points, one at high frequency ω^+, the other at low frequency, ω^-. Invoking the resonance condition $2k_wv_o=(\Omega_o/\gamma_o)\sqrt{1-f^2}$, and solving Eqs. (20) and (21), we find the radiation frequency:

$$\omega^{\pm} = 2k_wc\beta_o\gamma_o^2\Lambda(1 \pm \beta_oD) \tag{22}$$

where

$$\Lambda = 1 + (1/\sqrt{1-f^2}) \text{ and } D = \left[1 - (f^2/(1 + \sqrt{1-f^2})^2 - 1)\right]^{\frac{1}{2}}$$

In the limit $f \simeq 0$, Eq. (22) reduces to:

$$\omega^{\pm} \simeq 4k_wc\beta_o\gamma_o^2(1 \pm \beta_o) \tag{23}$$

which is similar to the radiation frequency of a conventional FEL. Since the resonance condition requires that $2k_wv_o=(\Omega_o/\gamma_o)\sqrt{1-f^2}$, we see that ω increases with Ω_o and thus increases with B_o, in agreement with measurements (see Figs. 6 and 7). This is unlike the computations of Ref. 4 in which the electric field of the wave is polarized so as to interact with the δv_y oscillatory motion (which is not resonantly enhanced). One then finds that ω decreases with increasing B_o.

To find the instability growth rate one must compute the imaginary part of the frequency from the full dispersion equation (18). A representative calculation is shown in Fig. 12 for the case of a tenuous beam ($f\simeq0$) with a spatial gaussian profile $n_o(x)$.

In the actual experiments described in section II the electron beam is

dense and close to Brillouin equilibrium. If f(x) is known (or assumed), Eq. (8) can be used to find the position x_r of the resonant layer. We have chosen f=0.8 which is close to Brillouin equilibrium. Then using the measured voltage-magnetic field characteristics shown plotted in Fig. 3 and allowing for self-electric and magnetic fields,[15,16] we compute the radiation frequency as a function of the axial magnetic field B_o. The solid lines shown in Fig. 7 for N=12 and 24 represent the results of these calculations. The agreement with experiment is seen to be fairly good. We note that increasing N from 12 to 24 does not change the radiation frequency appreciably.

IV. DISCUSSION

Experiments show that the rippled field magnetron is an intense source of coherent, narrow band radiation whose frequency can be tuned continuously by varying the axial magnetic field. Several hundred kilowatts of millimeter wave radiation has been observed in the frequency range from 25GHz to 50GHz.

The observed radiation frequency ω increases linearly with applied magnetic field B_o, and is almost independent of the wiggler wavenumber k_w. This differs from what may be expected from a conventional FEL based on the coupling of first order undulatory oscillations of the electrons with the radiation field. Such models[2,4] predict that ω scales linearly with k_w and <u>decreases</u> with increasing B_o.

In this paper we present a theoretical model different from those mentioned above.

Here we invoke a second order resonance $2k_w v_o = (\Omega_o/\gamma_o)\left[1-(\omega_p/\Omega_o)^2\right]^{\frac{1}{2}}$ in the electron motion which leads to radiation characteristics like those given by Eq.(22) and illustrated in Fig. 7. It is not known why the first-order, non-resonant FEL mode seen in other[7,8] circular FELs is not observed here.

Unfortunately, the aforementioned resonant interaction carries with it a penalty, namely the radiation frequencies are not as high as one might have

hoped. Consider, for example, a tenuous ($f \to 0$) relativistic electron beam ($\beta_o \to 1$). It then follows from Eqs. (8) and (23) that for the resonant interaction, $\omega_R^+ \simeq 4\Omega_o\gamma_o$, and the radiation frequency equals four times the nonrelativistic cyclotron frequency. This is to be compared with the nonresonant FEL radiation frequency given by $\omega_{NR}^+ \simeq 2k_w c\gamma_o^2$ and the relativistic cyclotron maser[17] frequency $\omega_c^+ \simeq 2\gamma_o^2\Omega_o$. In most practical systems, the two last named will exceed ω_R^+.

ACKNOWLEDGMENTS

This work was supported in part by the United Air Force Office of Scientific Research, in part by the National Science Foundation, and in part by the Department of Energy.

TABLE I. Summary of operating parameters of the rippled-field magnetron.

Radius of cathode	5.22 cm
Radius of anode	4.43 cm
Length of anode	6.0 cm
Voltage	0.7-1.5 MV
Current	1-20 kA
Pulse length	30 ns
Axial magnetic field	5-15 kG

TABLE II. Summary of the samarium-cobalt bar magnet assembly.

Total number of magnets	= 96
Magnet dimensions	= 0.40×0.40×4.8 cm
Residual induction, B_r	= 9.0 kG

Periodicity ℓ_w (cm)	N	Number of Magnets per Period	Field Amplitude B_{ow} (kG)
1.26	24	2	0.68
2.53	12	4	1.96

REFERENCES

1. P.A. Sprangle, R.A. Smith, and V.L. Granatstein, in Infrared and Submillimeter Waves, edited by K. Button (Academic, New York, (1979), Vol 1, p. 279 and references therein.

2. G. Bekefi, Appl. Phys. Lett. 40, 578 (1982).

3. R.C. Davidson, W. A. McMullin, and K. Tsang, Phys. Fluids 27, 233 (1984).

4. C-L. Chang, E. Ott, T.M. Antonsen, Jr., and A.T. Drobot, Phys. Fluids 27, 2937 (1984).

5. Y.Z. Yin and G. Bekefi, accepted for publication in Phys. Fluids.

6. G. Bekefi, R.E. Shefer, and B.D. Nevins, Lasers '82, Society for Optical and Quantum Electronics, SOQUE, 1982 (STS Press, McLean, Va.) 1982, p. 136.

7. G. Bekefi, R.E. Shefer, and W.W. Destler, Appl. Phys. Lett. 44, 280 (1984).

8. W.W. Destler, F.M. Aghamir, D.A. Boyd, G. Bekefi, R.E. Shefer, and Y.Z. Yin, accepted for publication in Phys. Fluids.

9. T.J. Orzechowski and G. Bekefi, Phys. Fluids 22, 978 (1979); and references therein.

10. K. Halbach, Lawrence Livermore Laboratory, University of California Accelerator and Fusion Research Division Report No. LBL11393, August 1980.

11. J.A. Pasour and S.P. Schlesinger, Rev. Scient. Instr. 48, 1355 (1977).

12. F. Hartemann, to be submitted as a thesis, Université Paris XI (unpublished).

13. P. Sprangle, J. Appl. Phys. 47, 2935 (1976).

14. W.P. Allis, S.J. Buchsbaum, and A. Bers, "Waves in Anisotropic Plasma" (MIT Press 1963) p. 184.

15. J. Swegle and E. Ott. Phys. Fluids 24, 1821 (1981).

16. R.C. Davidson, K.T. Tsang, and J. Swegle, Phys. Fluids 27, 2332 (1984).

17. R.E. Shefer and G. Bekefi, Int. J. Electronics 51, 569 (1981).

FIGURE CAPTIONS

Fig. 1. Schematic diagram of the rippled-field magnetron.

Fig. 2. Experimental arrangement.

Fig. 3. Typical current voltage characteristics as a function of the external magnetic field B_o, for N=12.

Fig. 4. Total power emitted in the K_a-band range of frequencies; N=12.

Fig. 5. Spectral characteristics with and without wiggler, obtained with a millimeter-wave grating spectrometer; N=12.

Fig. 6. Radiation frequency as a function of the external magnetic field B_o, for N=12. Open circles represent spectrometer measurements, and solid dots are dispersive line measurements.

Fig. 7. Radiation frequency as a function of the external magnetic field B_o for N=12 and 24. The dots represent dispersive line measurements. The lines are from theory (see section III).

Fig. 8. Planar version of the rippled-field magnetron.

Fig. 9. Computer simulation of the motion of an electron in the crossed-field FEL static fields, far from resonance (top), and near resonance (bottom). ℓ_w=1.0cm, E_o=1.0MV cm^{-1}. B_o=6.00kG (top), and 9.05kG (bottom); B_{ow}=1.0kG.

Fig. 10. Computer simulation showing the resonance in particle velocity as a function of the externally applied magnetic field B_o. ℓ_w=1.0cm, E_o=0.5MV cm^{-1}; B_{ow}=1.0kG.

Fig. 11. Schematic diagram of the dispersion relation of the interacting waves.

Fig. 12. Real and imaginary parts of the radiation frequency for the case of a tenuous beam at resonance with a gaussian profile $n_o(x) = n_o \exp\left[-\left((x-x_o)/\delta x\right)^2\right]$; $f^2(x_o)=0.01$, $R=1.0$, $\delta x=0.25$cm. The normalized growth rate is in units of $\mathrm{Im}(\omega)/\omega_p$.

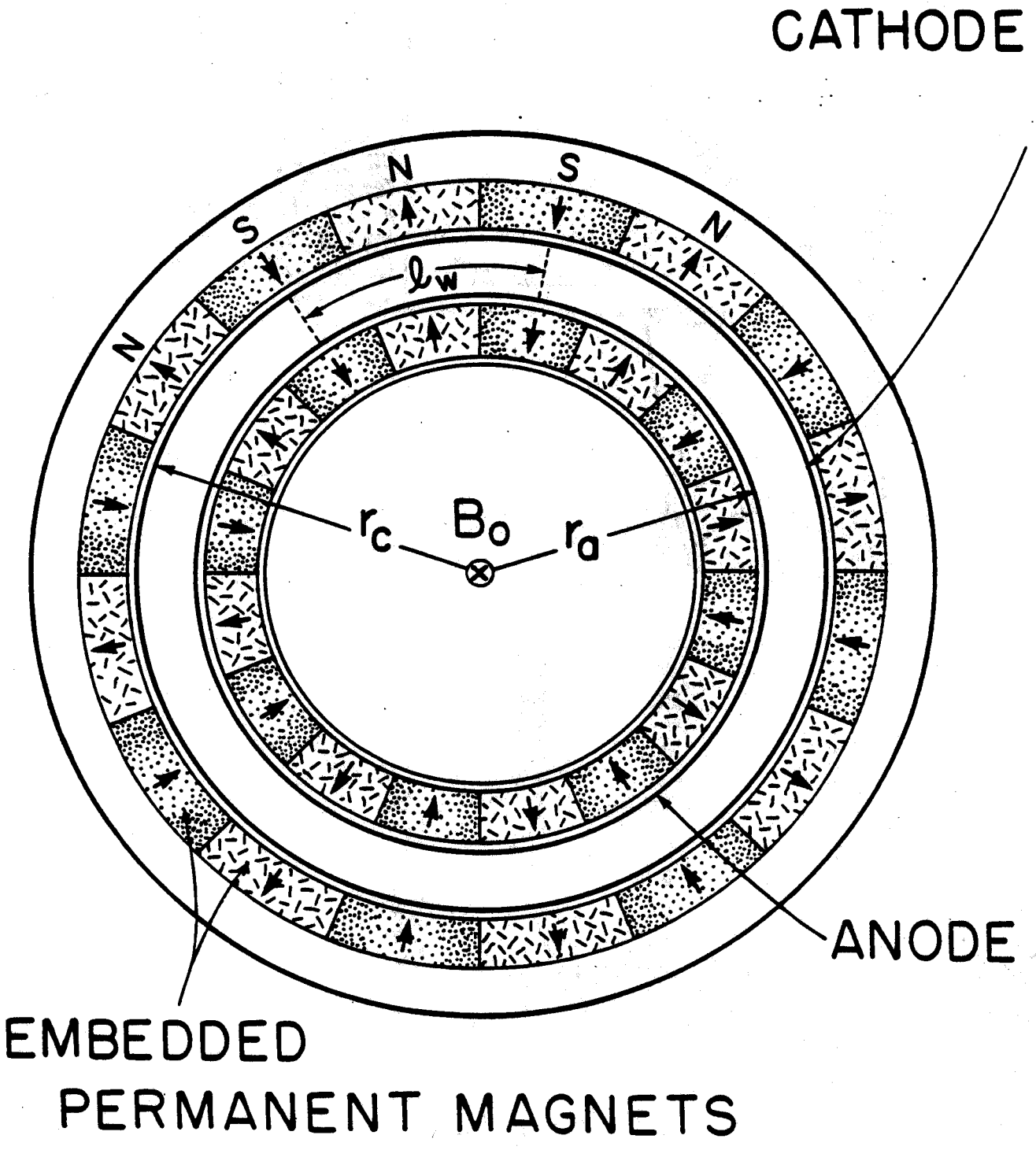

Fig. 1
Hartemann, Bekefi, Shefer

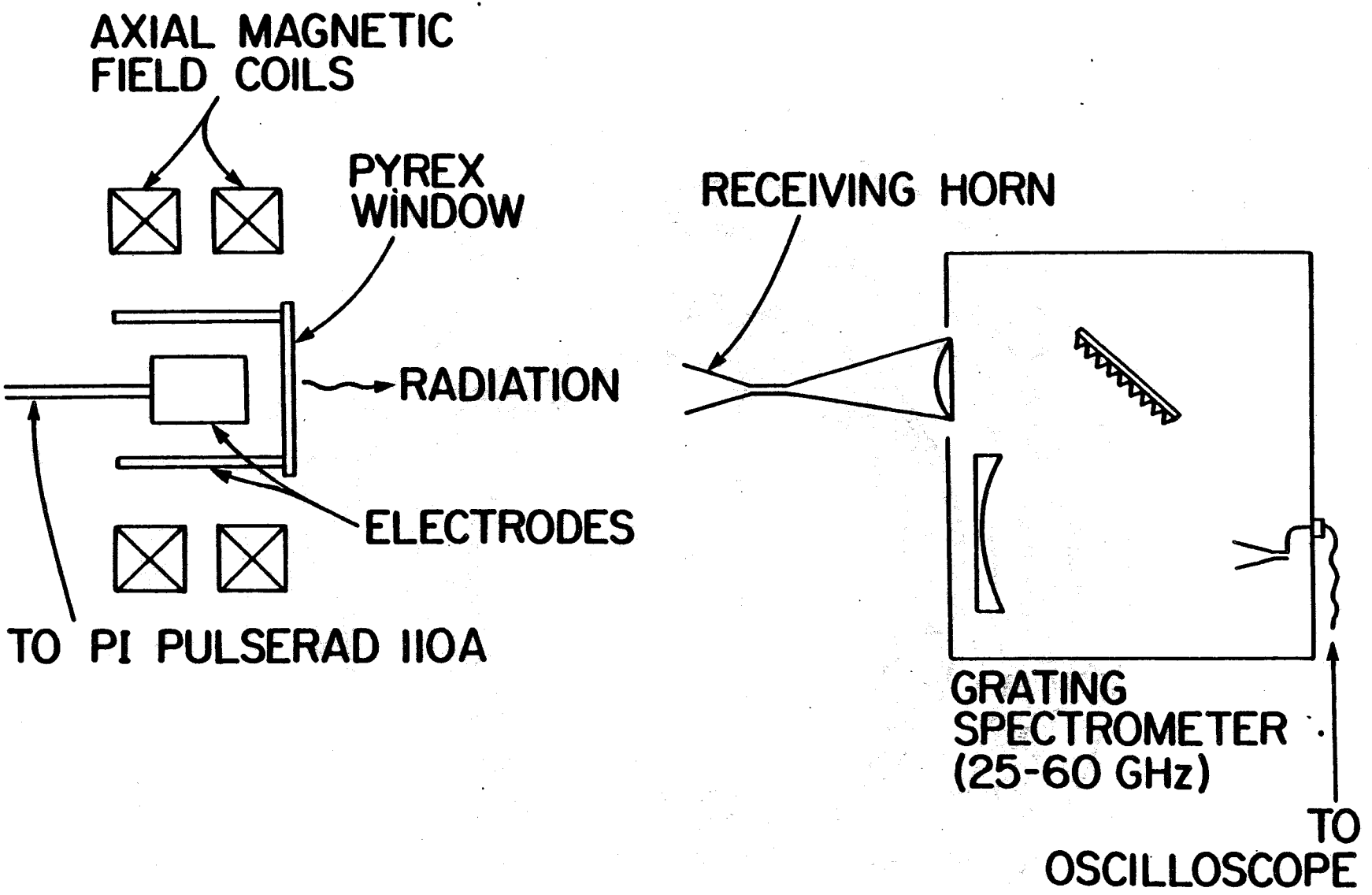

Fig. 2
Hartemann, Bekefi, Shefer

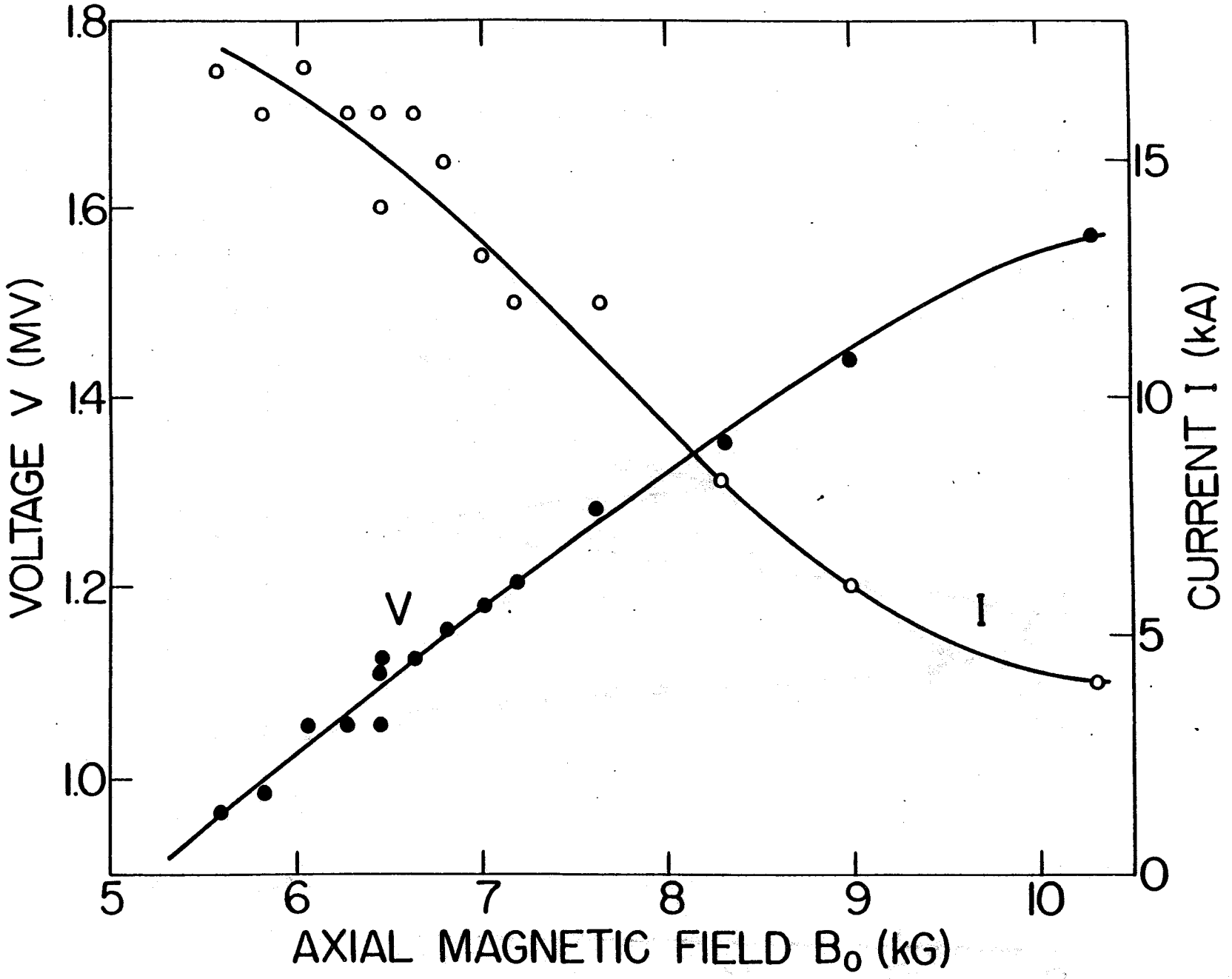

Fig. 3
Hartemann, Bekefi, Shefer

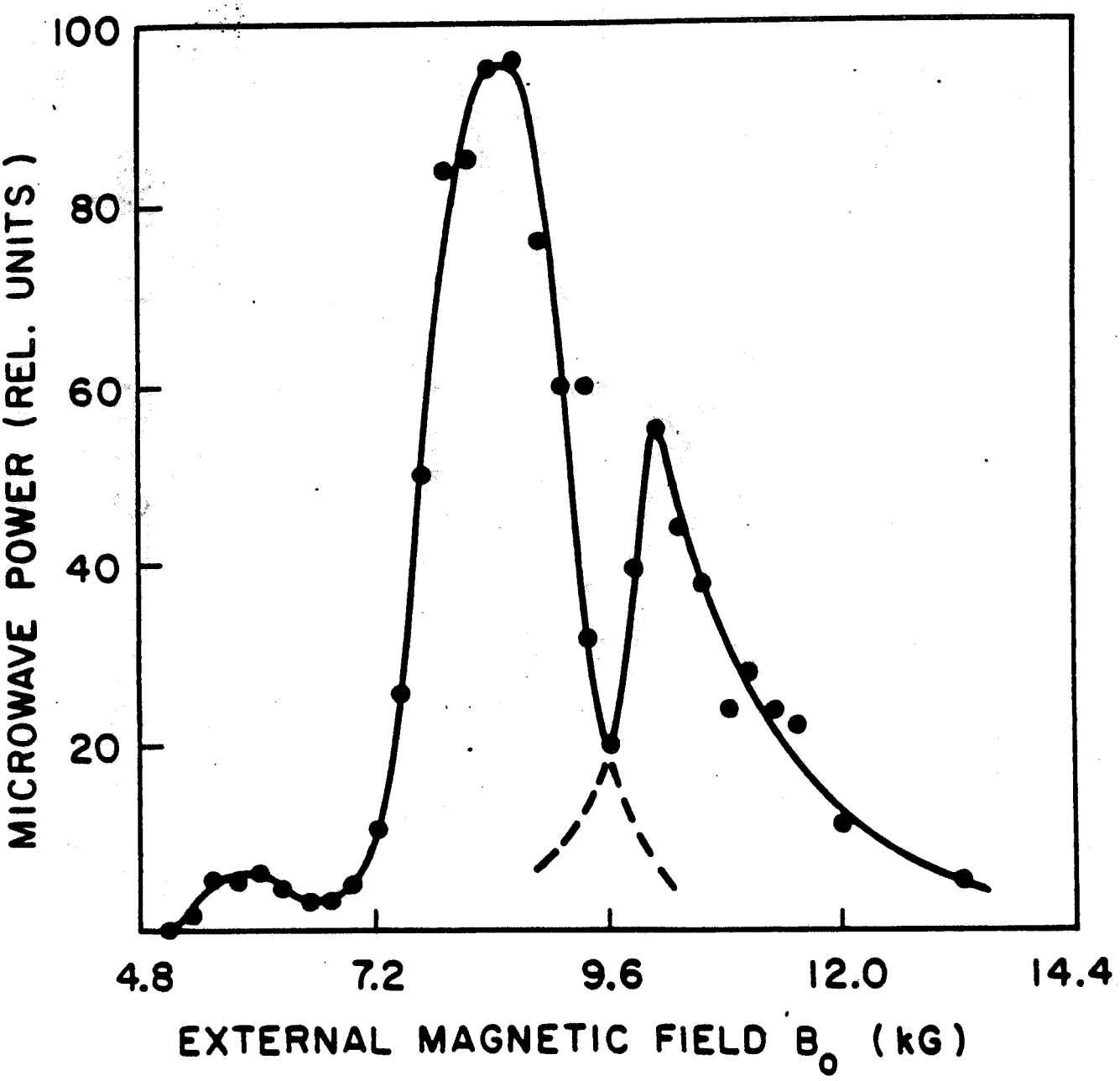

Fig. 4
Hartemann, Bekefi, Shefer

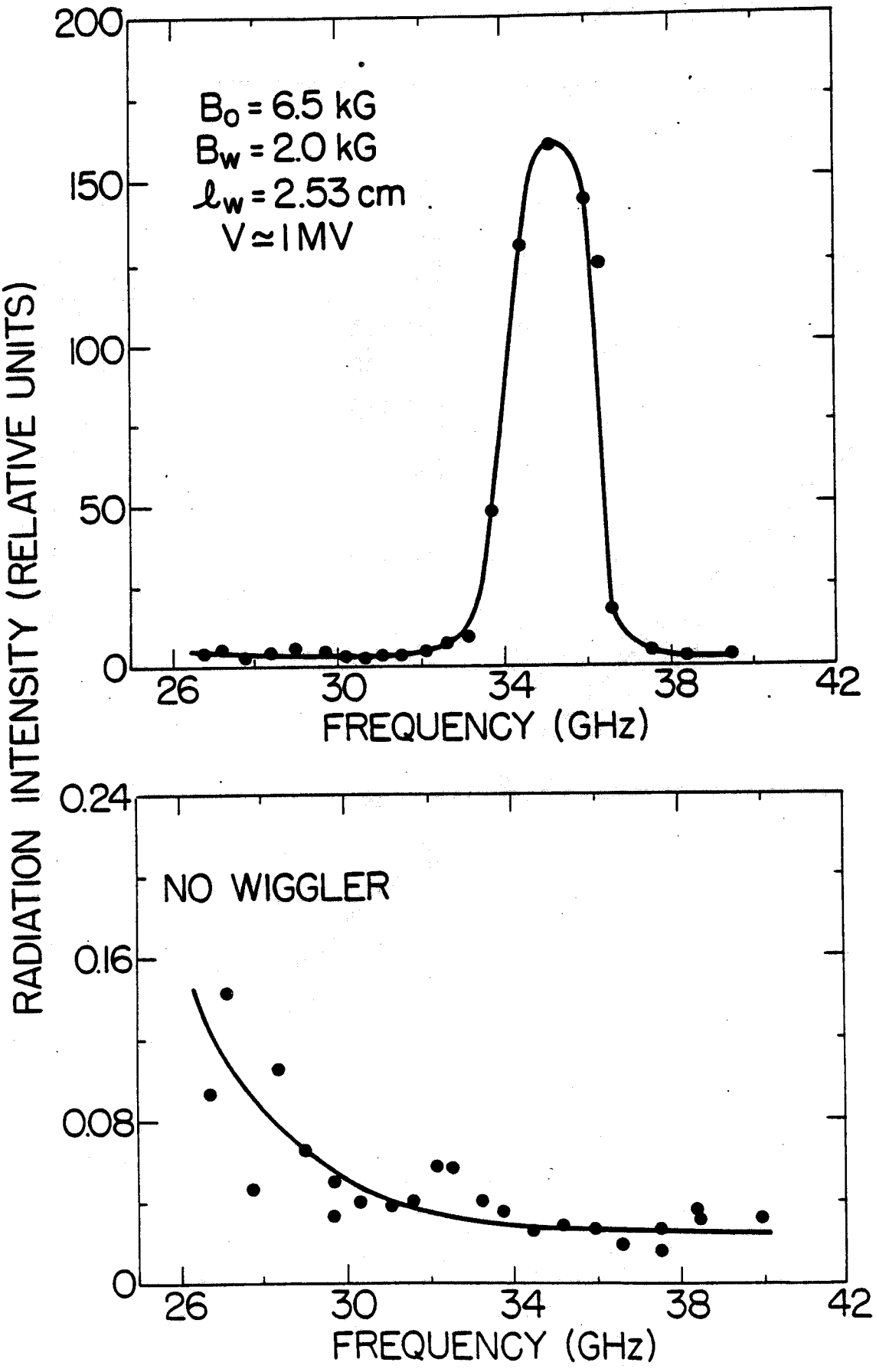

Fig. 5
Hartemann, Bekefi, Shefer

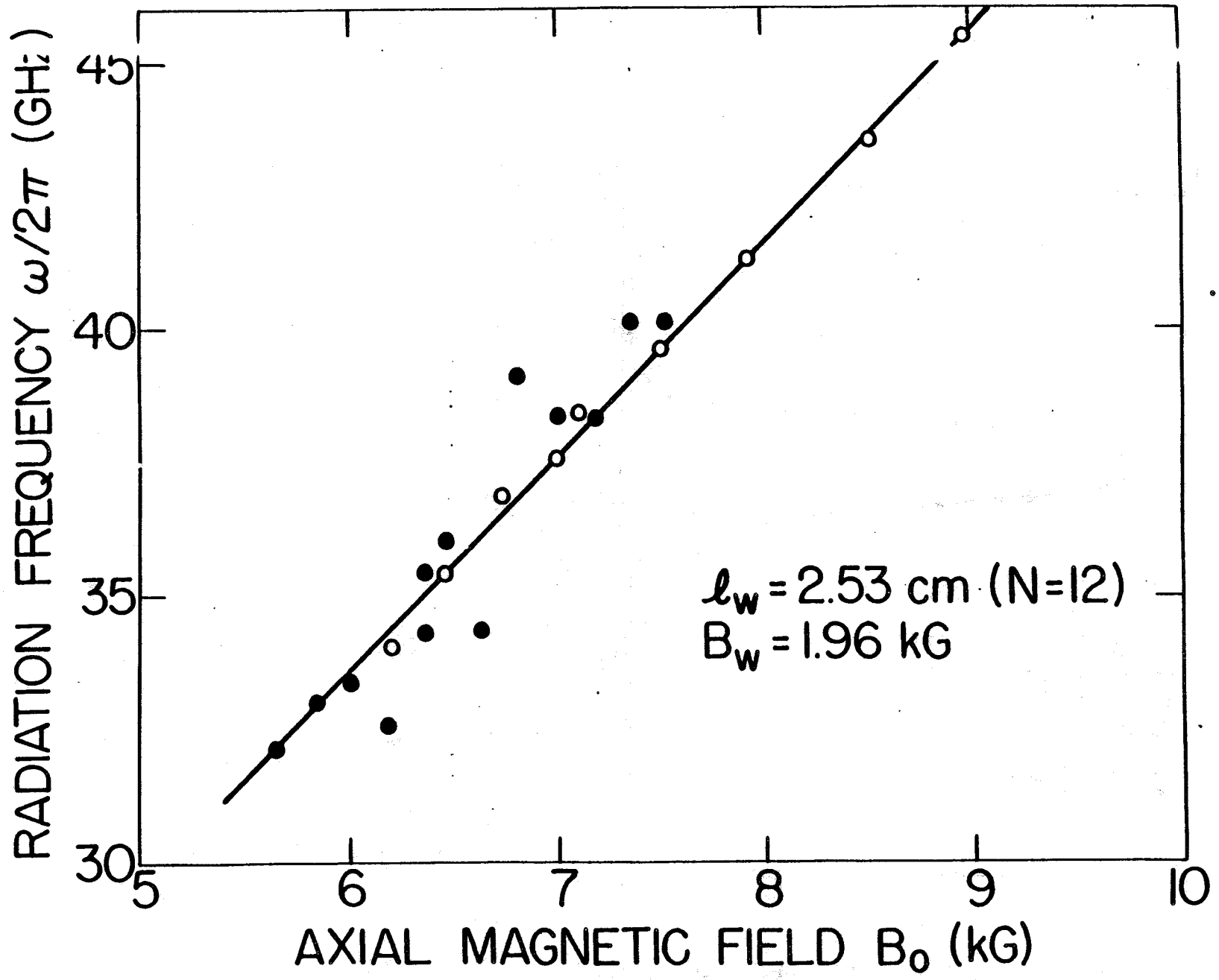

Fig. 6
Hartemann, Bekefi, Shefer

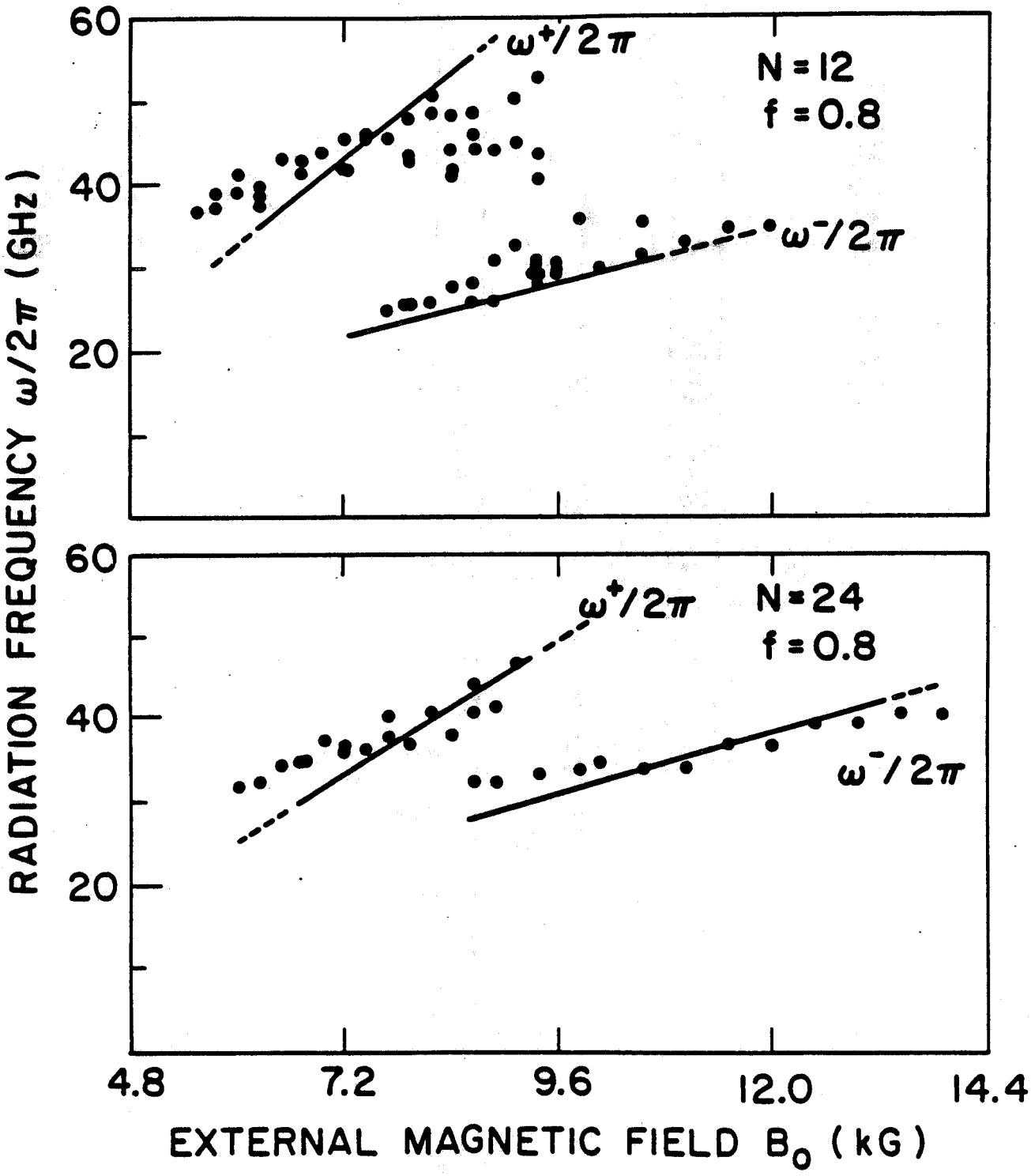

Fig. 7
Hartemann, Bekefi, Shefer

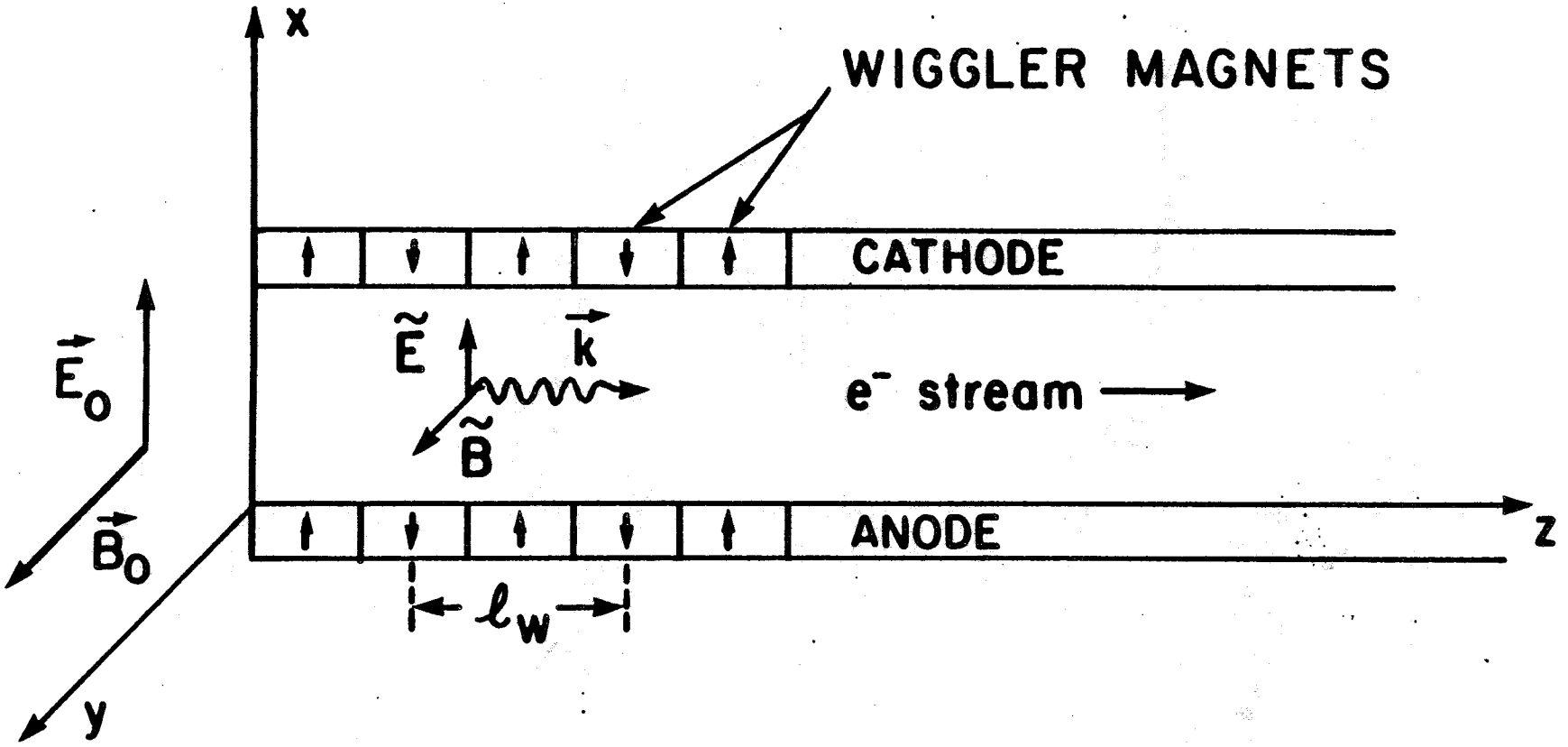

Fig. 8
Hartemann, Bekefi, Shefer

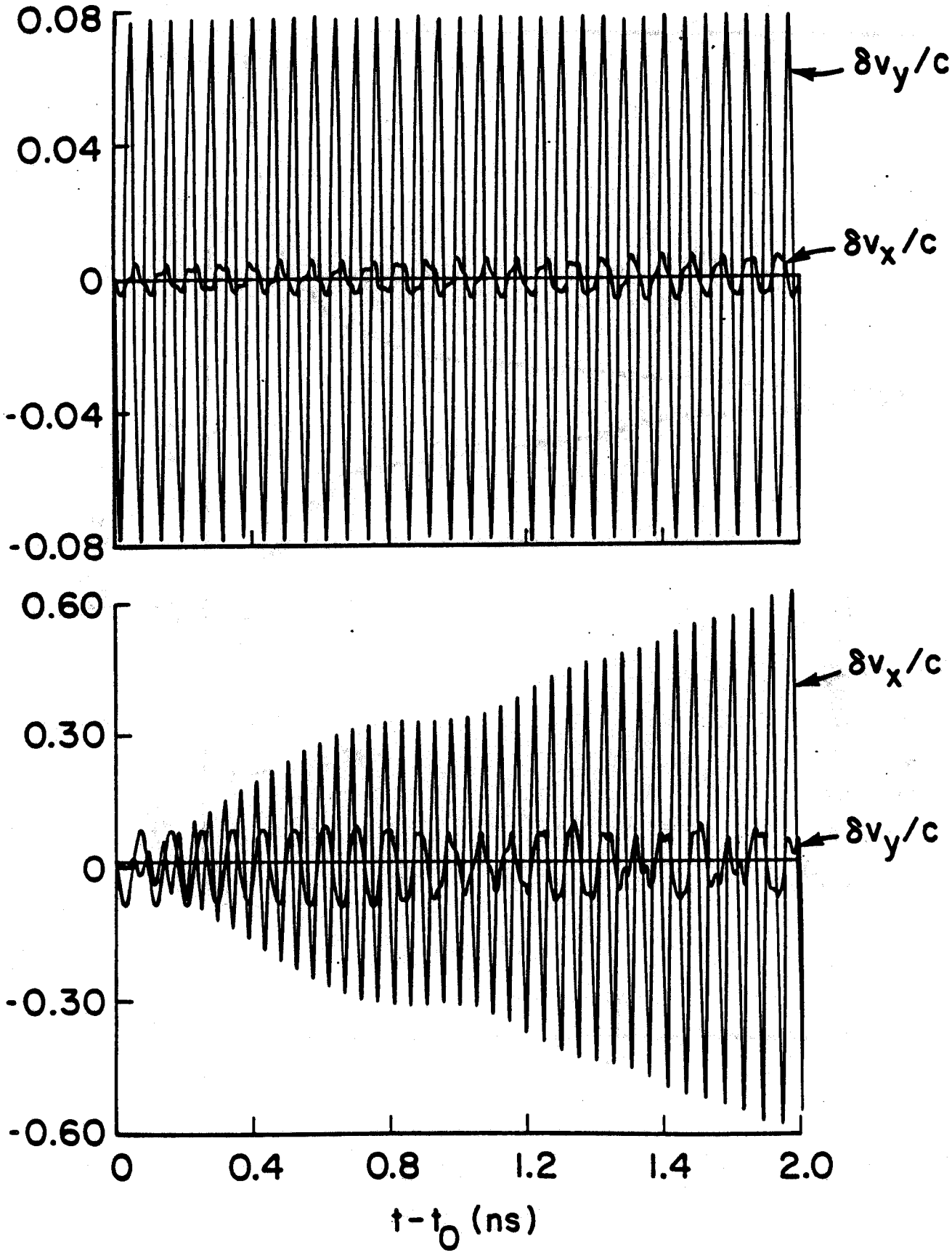

Fig. 9
Hartemann, Bekefi, Shefer

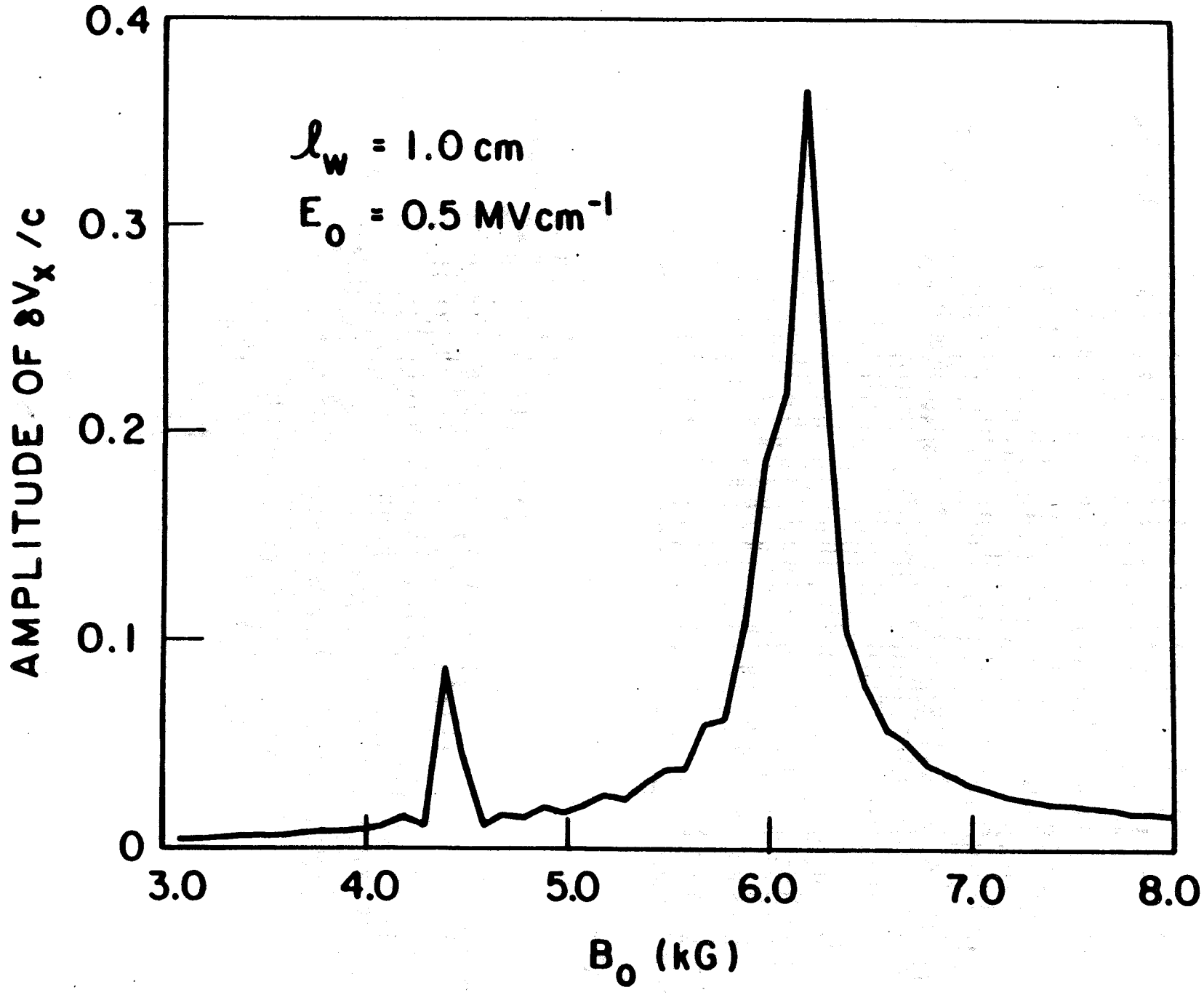

Fig. 10
Hartemann, Bekefi, Shefer

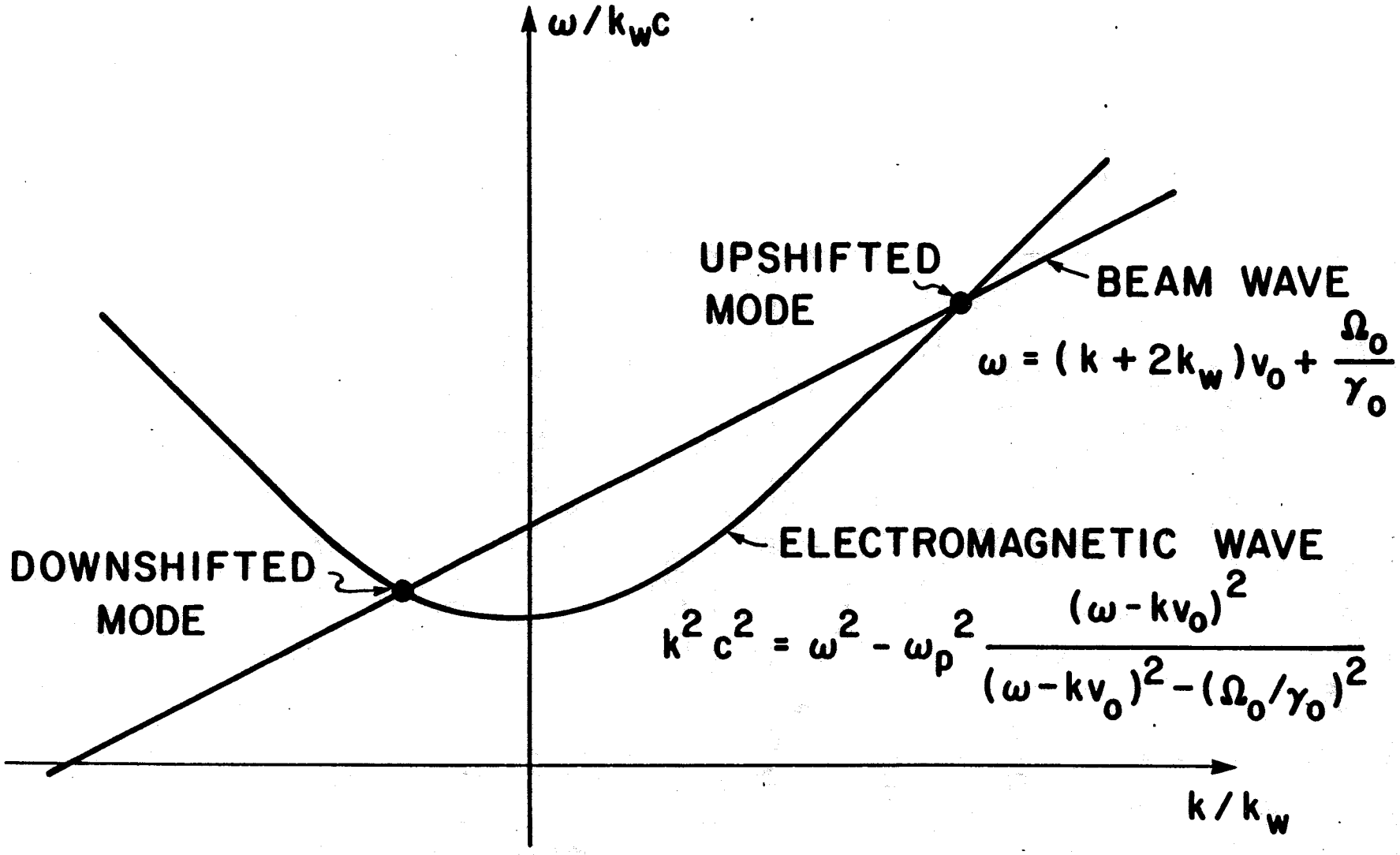

Fig. 11
Hartemann, Bekefi, Shefer

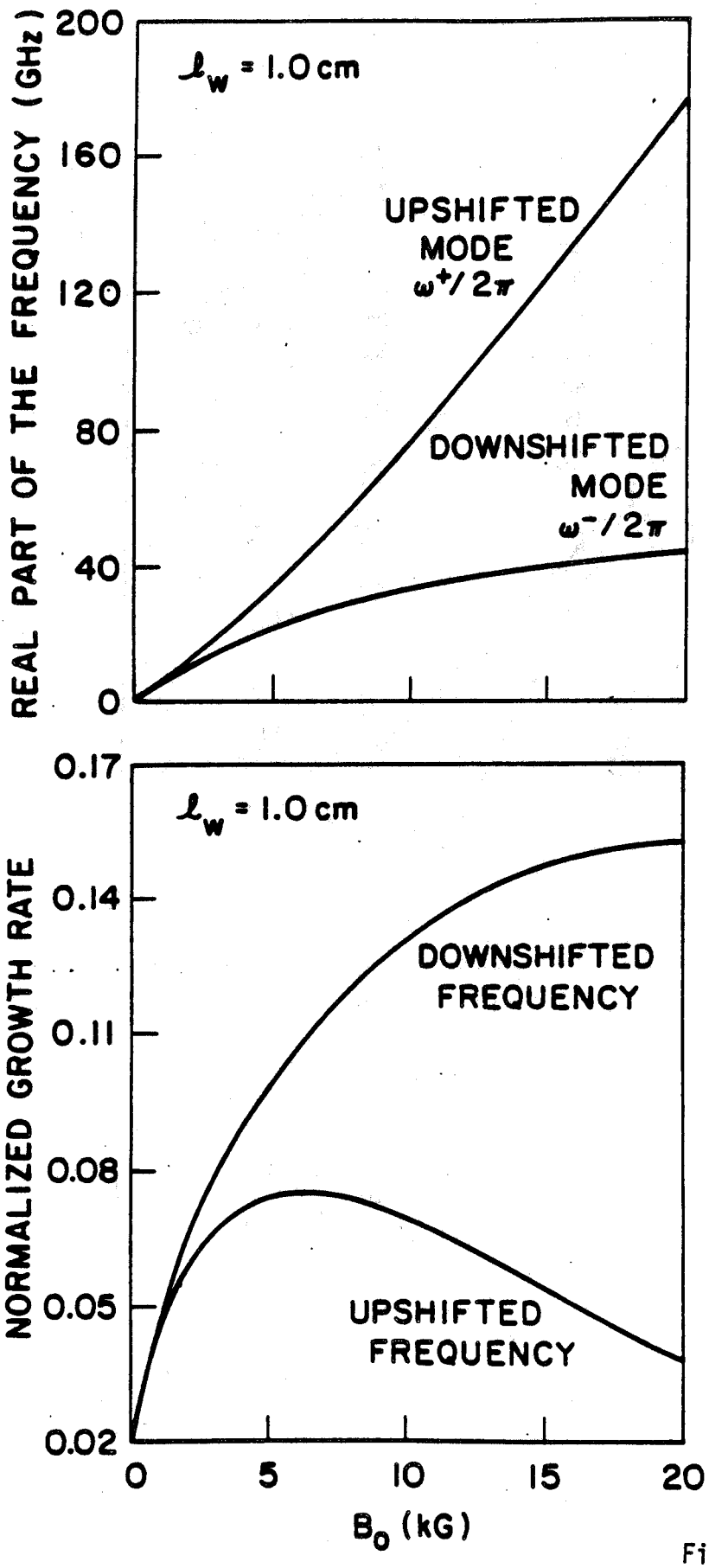

Fig. 12
Hartemann, Bekefi, Shefer